

Reversible Trapping of Colloids in Microgrooved Channels via Diffusiophoresis under Steady-State Solute Gradients

Naval Singh,¹ Goran T. Vladislavljević,¹ François Nadal,² Cécile Cottin-Bizonne,³ Christophe Pirat,³ and Guido Bolognesi^{1,*}

¹*Department of Chemical Engineering, Loughborough University, Loughborough, LE11 3TU, United Kingdom*

²*Wolfson School of Mechanical, Electrical and Manufacturing Engineering, Loughborough University, Loughborough, LE11 3TU, United Kingdom*

³*Institut Lumière Matière, UMR5306 Université Claude Bernard Lyon 1 - CNRS, Université de Lyon, Villeurbanne Cedex, 69622, France*

(Dated: November 20, 2020)

The controlled transport of colloids in dead-end structures is a key capability that can enable a wide range of applications, such as bio-chemical analysis, drug delivery and underground oil recovery. This letter presents a new trapping mechanism that allows the fast (i.e., within a few minutes) and reversible accumulation of sub-micron particles within dead-end micro-grooves by means of parallel streams with different salinity level. For the first time, particle focusing in dead-end structures is achieved under steady-state gradients. Confocal microscopy analysis and numerical investigations show that the particles are trapped at a flow recirculation region within the grooves due to a combination of diffusiophoresis transport and hydrodynamic effects. Counterintuitively, the particle velocity at the focusing point is not vanishing and, hence, the particles are continuously transported in and out of the focusing point. The accumulation process is also reversible and one can cyclically trap and release the colloids by controlling the salt concentration of the streams via a flow switching valve.

Particle transport in confined structures plays an important role in several technological applications, including drug delivery, diagnostics, enhanced oil recovery, particle separation and filtration technologies. Nevertheless, the implementation of an effective strategy for controlling the motion of colloidal particles within a confined environment, such as a dead-end channel or a porous medium, is still a challenging and thought-provoking task. In recent years, an increasing number of studies have exploited the motion of particles and liquids induced by solute concentration gradients — the so-called diffusiophoresis (DP) and diffusioosmosis (DO) phenomena — to enable particle manipulation capabilities, such as delivery to/extraction from dead-end pores [1–3], particle focusing [4–8] and separation [9–11]. In DP with electrolytes, the motion of a particle is driven by a solute concentration gradient ∇c and the resulting particle velocity can be expressed as $\mathbf{u}_{\text{DP}} = \Gamma_{\text{DP}} \nabla \ln c$, with the DP coefficient Γ_{DP} being a function of the particle and solution properties [12]. Externally applied unsteady solute gradients have been adopted to boost the otherwise slow and diffusion-limited migration of nano-/micro-particles within dead-end structures [1–3]. However, due to the transient nature of the imposed gradients, the particle and flow manipulation capabilities are lost within a short period of time (typically, few tens of minutes). The ability to generate a steady-state solute gradient within dead-end structures and, hence, retain indefinitely the particle manipulation capability has yet to be achieved. On the other hand, steady-state solute gradients have been used to accumulate colloids in target locations within microfluidic chambers and open-ended microchannels. For

instance, steady-state gradients of chemically reactive solutes [6] can induce particle focusing at the location where $\mathbf{u}_{\text{DP}} = 0$. Alternatively, particle focusing can be achieved also by counteracting the DP particle migration with a hydrodynamic flow, \mathbf{u} , that advects the particles in the opposite direction [7, 8, 11]. As a result, particle accumulation occurs at the regions where the particle's total velocity, $\mathbf{u}_{\text{p}} = \mathbf{u} + \mathbf{u}_{\text{DP}}$, vanishes. For sub-micron particles, however, their slow Brownian diffusion cannot compete with the particle velocity \mathbf{u}_{p} and, thus, the particle concentration increases indefinitely until the packing limit is reached and the microchannels are irreversibly clogged [7].

Here, we report a new focusing mechanism through which sub-micron particles can be rapidly and reversibly accumulated within dead-end structures (microgrooves) by means of a steady-state gradient. In contrast with other focusing strategies, a steady-state particle distribution is achieved within a few minutes meanwhile the concentration peak remains well below the packing limit, thereby avoiding irreversible effects such as particle clustering and device clogging. The particle accumulation process is hence fully reversible and colloids can be transported into and out of the grooves multiple times by switching between different flow streams.

To create a steady-state solute gradient, parallel flows are injected into a Ψ -shaped microchannel, made of an optical adhesive (NOA81) glued on top of a silicon substrate with transverse microgrooves, as schematically shown in Fig. 1(a) — see Supplementary Information (SI) for details on the device fabrication [13]. A total of 1250 grooves are evenly distributed along the

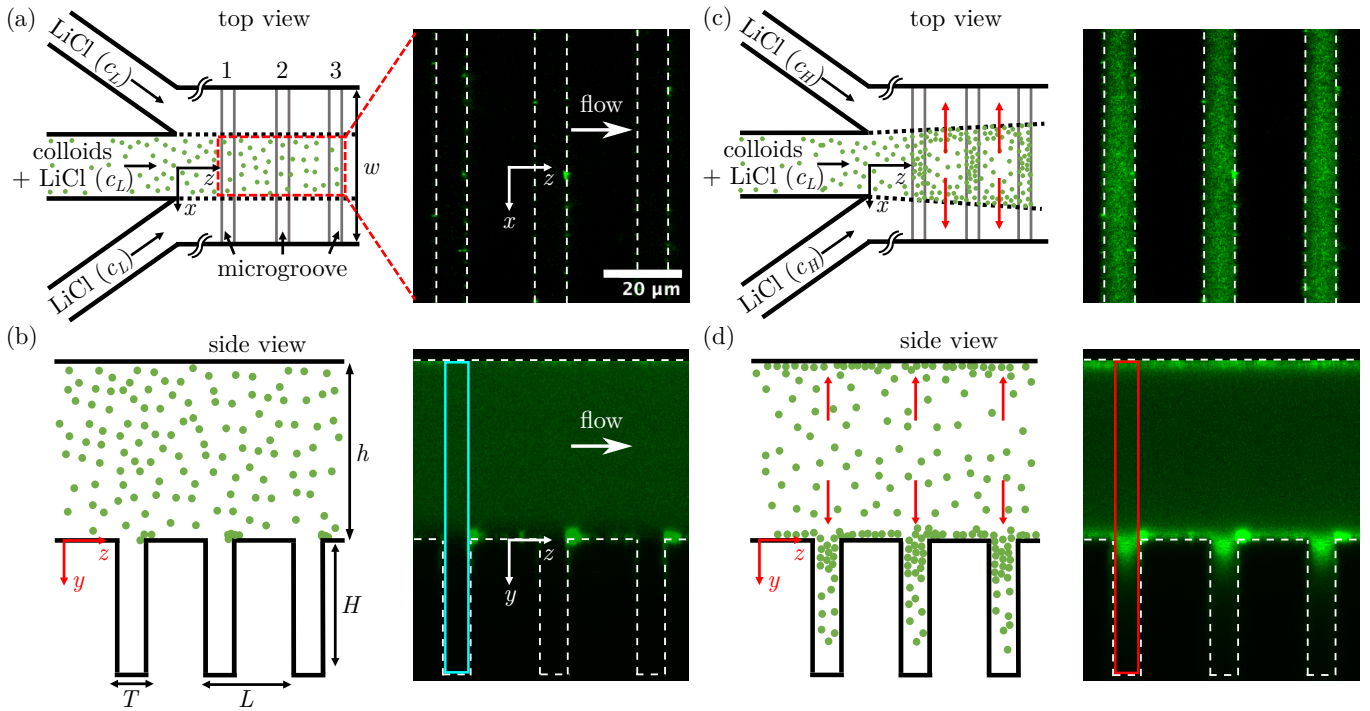


FIG. 1. Solute-induced particle trapping in microgrooves under steady-state conditions. (a, b) Schematics of top and side view of the device and corresponding fluorescence micrographs of three grooves located at 4 mm from the junction *without* solute contrast. Outer flow: LiCl in DI water at low concentration, $c_L = 0.1$ mM. Inner flow: colloids (215 nm in diameter @ 0.025% v/v) + LiCl in DI water at low concentration c_L . (c, d) Schematics and micrographs as in panels (a) and (b) *with* solute contrast. Outer flow: LiCl in DI water at high concentration, $c_H = 10$ mM. Inner flow: colloids + LiCl in DI water at low concentration, c_L . Red arrows show the direction of the salt gradient. White dashed lines represent channel boundaries and groove edges. Channel size: width $w = 400$ μm , depth $h = 57$ μm . Groove size: thickness $T = 8$ μm , depth $H = 45$ μm , pitch $L = 32$ μm . In (a) and (c), fluorescence intensities are averaged along the channel depth direction y , whereas in (b) and (d) intensities are averaged over the width direction x . The same color scale applies to all micrographs. Blue and red rectangles show the integration windows over which the particle concentration profiles in Fig.2 are calculated.

4 cm length of the device. The inner flow is a suspension of carboxylate polystyrene fluorescent colloids (Fluoresbrite[®] YG, 0.20 μm , Polysciences) at a concentration of $n_0 = 0.025\%$ v/v, dispersed in a water (Ultra-pure Milli-Q) solution of LiCl (Acros Organics, 99%) at low concentration, $c_L = 0.1$ mM. The outer flow is a LiCl solution at either low concentration c_L (Fig. 1a-b) or high concentration $c_H = 10$ mM (Fig. 1c-d). Both the inner and outer flow rates are equal to 12.5 $\mu\text{L}/\text{min}$, resulting in an average speed U_0 of 18.3 mm/s. The 3D distribution of particles in the channel and the grooves is measured via laser scanning confocal microscopy as detailed in SI. In the absence of salt contrast, the colloidal particles hardly penetrate the grooves likely due to steric and electrokinetic wall-exclusion effects [2, 14], which keep most of the particles away from the grooved substrate (Fig. 1b). In presence of a salt contrast, the particles are expected to migrate towards region at a higher salt concentration, since the DP coefficient of the particles, Γ_{DP} , is positive (see SI for the evaluation of Γ_{DP}). A higher salt concentration in the outer flow streams generates a solute gradient along the channel width direction (x axis)

— see red arrows in Fig. 1(c) — which leads to colloid spreading along the same direction, as also previously reported in a similar flow configuration [4]. More interestingly, salt gradients arise also along the depth direction (y axis) — see red arrows in Fig. 1(d) — thereby dragging the particles towards the channel's top flat wall and inside the grooves. The y -component of the salt gradient is originated by the Poiseuille-like velocity profile in the rectangular channel. Indeed at distances z from the junction much smaller than $U_0 h^2 / D_s \simeq 4$ cm — with D_s the salt diffusivity — the salt diffusion process is affected by the non-uniform velocity profile along the channel depth, and the width of the salt diffusive zone at the interface between the inner and outer flows decreases with the distance from the top and bottom walls [15]. Consequently, in the inner region of the channel (i.e., $|x|/w < 0.5$) a solute gradient directed from the bulk towards the walls is established. It is worth noting that the DP migration of charged particles towards the channel walls in a parallel flow configuration has never been reported before and it could be exploited as a charge-based particle focusing/filtration strategy in microdevices with flat

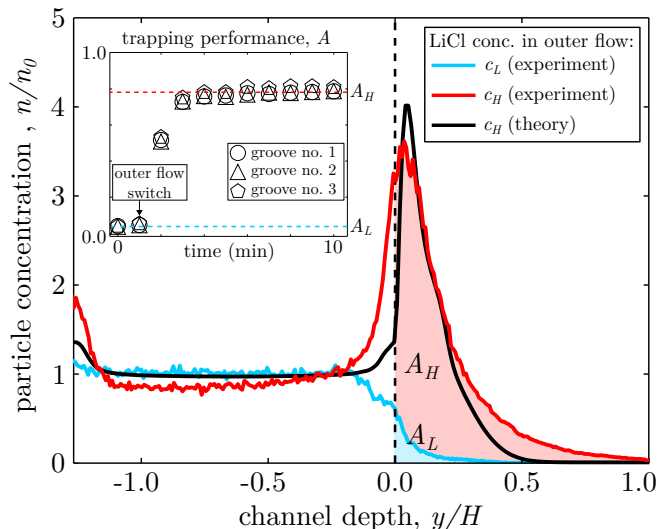


FIG. 2. Experimental steady-state particle concentration profiles along the channel depth *without* salt gradient (blue curve) and *with* salt gradient (red curve), corresponding to the blue and red integration windows in Fig.1(b) and Fig.1(d), respectively. A_L and A_H are the integral of the profiles within the groove ($y \geq 0$) without and with salt gradient, respectively. The profile (black curve), predicted by the numerical simulation in presence of salt gradient, is also shown. Inset: trapping performance of three neighboring grooves, at 4 mm from the junction, as outer flow is switched from low ($c_L = 0.1$ mM) to high ($c_H = 10$ mM) salt concentration.

walls only. Driven by DP, the particles migrate towards the grooves and accumulate at the groove's entrance as shown in Fig. 1(c-d).

Fig. 2 shows the steady-state colloid concentration profiles along the depth direction, with salt gradient (red line) and without salt gradient (blue line), for groove 1 in Fig. 1. The 3D colloid concentration field $n(x, y, z)$ are calculated from the fluorescence intensity of the confocal scan images via a calibration curve (see Fig. S2). The concentration profiles in Fig. 2 are calculated for each groove by averaging $n(x, y, z)$ over the x range of the confocal images (ca. $x/w \in [-0.2, 0.2]$) and over the z range corresponding to the groove thickness T , as highlighted by the solid rectangles in the side-view micrographs shown in Fig. 1(b,d). As shown in Fig. 2, the salt contrast between the parallel streams induces the particle migration from the channel bulk towards the top flat wall ($y \rightarrow -h$) and the groove ($y > 0$), whereas a slight decrease of particle concentration in the bulk ($n < n_0$) is observed. By definition, the area A below the profile curves for $y > 0$ (shaded regions) corresponds to the average particle concentration within the groove, normalized with respect to n_0 . The parameter A can be hence used as a measure of the groove trapping performance. The inset in Fig. 2 shows the evolution of the trapping performance, A , for the three consecutive grooves shown in Fig. 1, as the outer flow is switched, at the arbitrary time

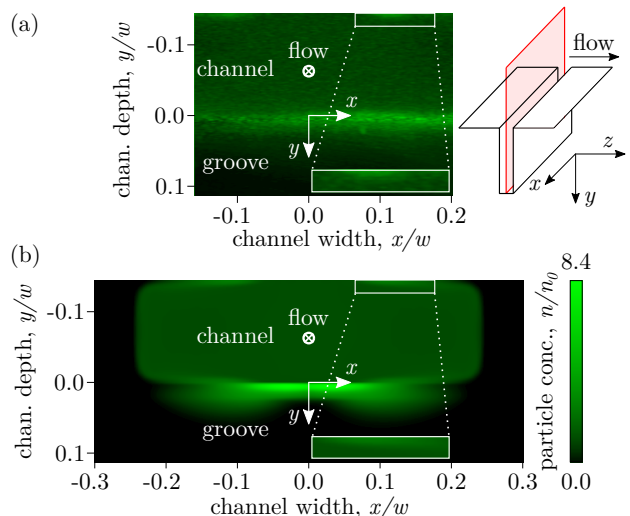


FIG. 3. Experimental (a) and simulated (b) steady-state particle distribution on a plane perpendicular to the flow direction, corresponding to the red-shaded region in the cartoon, at 4 mm from the junction and with a solute gradient ($c_L = 0.1$ mM and $c_H = 10$ mM). Fluorescence intensities (a) and simulated particle concentration (b) are averaged over the groove thickness T (along the z axis). The close-ups highlight one of the two focusing regions near the top flat wall.

$t = 1$ min, from low (c_L) to high (c_H) salt concentration solution by means of a flow switching valve. In few minutes, the value of A increases from $A_L = 0.022 \pm 0.002$ to $A_H = 0.79 \pm 0.03$ at steady-state, thereby resulting in ca. 36 fold increase in the average particle concentration within the grooves.

To shed light on the mechanisms governing the particle trapping, a numerical analysis (see SI for details) is performed in Comsol Multiphysics to simulate the particle concentration field. The 3D computational domain consists of a rectangular channel and a single groove at 4 mm from the junction. A slip velocity, $\mathbf{u}_s = -\Gamma_{\text{DO}} \nabla \ln c$, with Γ_{DO} the diffusioosmosis coefficient, is imposed at the domain walls whereas the velocity of the particles \mathbf{u}_p is defined as the sum of the hydrodynamic velocity and DP velocity, $\mathbf{u}_p = \mathbf{u} + \mathbf{u}_{\text{DP}}$. The value of Γ_{DO} for the channel walls could not be measured so this parameter is adjusted in order to achieve a good match between experimental and numerical results (see SI). The colloid concentration profile along the channel depth predicted by the numerical simulation — shown as a black curve in Fig.2 — compares well with the experimental profile (red curve). The good agreement between experiments and theoretical predictions is confirmed also by the experimental and simulated particle concentration field on a plane perpendicular to the flow direction, shown in Fig.3 (a) and (b), respectively. These cross-section views show that the salt gradient leads to the accumulation of particles just below the groove entrance

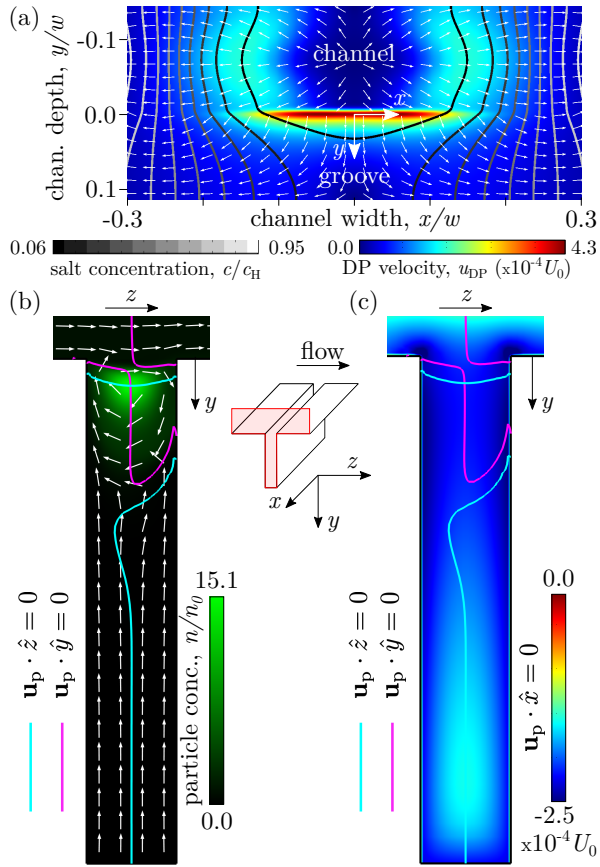


FIG. 4. Numerical simulation results. (a) DP velocity intensity and streamlines, and salt concentration isolines at the same x - y cross section as in Fig. 3. (b) Particle concentration and streamlines of the particle velocity \mathbf{u}_p at y - z cross section, $x/w = 0.03$, corresponding to the red-shaded region in the cartoon. (c) Out-of-plane component of \mathbf{u}_p at the same cross section of panel (b). The blue (magenta) solid lines show the points where the z -component (y -component) of \mathbf{u}_p vanishes.

as well as the formation of two symmetric and weaker focusing regions, nearly $0.2w$ ($\simeq 80 \mu\text{m}$) apart from each other, close the top flat wall (see insets). Indeed, in the region $|x|/w < 0.5$, the particles are transported towards the outer flow as well as the top and bottom walls by the DP velocity field \mathbf{u}_{DP} , shown in Fig. 4(a). As anticipated, in the channel the salt concentration isolines, also shown in Fig. 4(a), are bent towards the outer flow due to the Poiseuille-like hydrodynamic velocity profile. To clarify why particles accumulate only at the groove entrance without traveling further deep, one should look at the particle distribution together with the streamlines of the velocity field \mathbf{u}_p at a cross section perpendicular to the channel widthwise direction. Fig. 4(b) shows such a plot for the y - z cross section, $x/w = 0.03$, where the maximum particle concentration is achieved ($n_{\text{max}}/n_0 \simeq 15$). It can be seen that the hydrodynamic field \mathbf{u} is characterized by a recirculation region at the groove entrance and

a DO-induced flow with opposite direction with respect to the particle DP velocity, i.e. outwards of the groove. Therefore, as the particles migrate towards the groove by DP, they are captured by the closed flow streamlines in the recirculation region and accumulate at the center of the recirculation pattern where the in-plane (y and z) components of \mathbf{u}_p vanish. However, the DP migration further down the groove is counteracted by the DO flow in the opposite direction. Importantly, in the absence of DO, the particles would still accumulate within the recirculation region, but they would also concentrate at the bottom end of the groove due to DP transport (Fig. S4). It can be concluded that the observed particle trapping is due to the combined effects of DP particle migration and hydrodynamic flow recirculation within the groove. Despite both DO and Brownian diffusion affects the intensity of the particle concentration peak (i.e., n_{max}/n_0), they are not required to achieve particle trapping at the groove entrance. Most interestingly, the out-of-plane (x) component of particle velocity, $u_{p,x}$ at the examined y - z cross section is non-zero everywhere in the groove, as shown by Fig. 4(c). Consequently, the particles accumulate at a focusing point where the total particle velocity \mathbf{u}_p is non-vanishing and, thus, they are continuously transported in and out of the peak region. The 3D streamlines of the particle velocity field can be seen in Fig. S3. It is worth noting that \mathbf{u}_p vanishes at the center of the flow recirculation at the y - z cross section $x = 0$, since $u_{p,x} = 0$ due to symmetry. Counterintuitively, in the examined system the particle concentration peak is not achieved at that position despite $\mathbf{u}_p = 0$ and $\nabla \cdot \mathbf{u}_p < 0$. Note that the latter relation is a necessary condition for particle focusing (see derivation in SI), whereas the former is neither necessary nor sufficient for focusing to occur.

Our physical interpretation of the trapping mechanism is validated also by the fact that the simulation predicts a location of the peak in the particle concentration profile along the channel depth (Fig.2) at $y/H = 0.052$, which agrees very well with the peak location observed in the experiments (i.e., $y/H = 0.051 \pm 0.003$). Furthermore, the trapping efficiency, $A = 0.69$, in the simulations compares well with the one calculated from experiments ($A = 0.79 \pm 0.03$).

Upon removal of the salt gradient, the trapping mechanism ceases and the particles can freely diffuse out of the grooves. Such an effect allows one to control the delivery and extraction of particles into and from the grooves by simply adjusting the salinity contrast between the inner and outer flows. This capability is confirmed by the experimental results, shown in Fig. 5, where the outer flow is alternated between two LiCl solutions of $c_L = 0.1 \text{ mM}$ and $c_H = 10 \text{ mM}$. As the flow configuration is cycled between iso-osmotic ($t = 0, 20, 40 \text{ min}$) and salt gradient ($t = 10, 30 \text{ min}$) conditions, the colloid concentration profile and the groove trapping performance change ac-

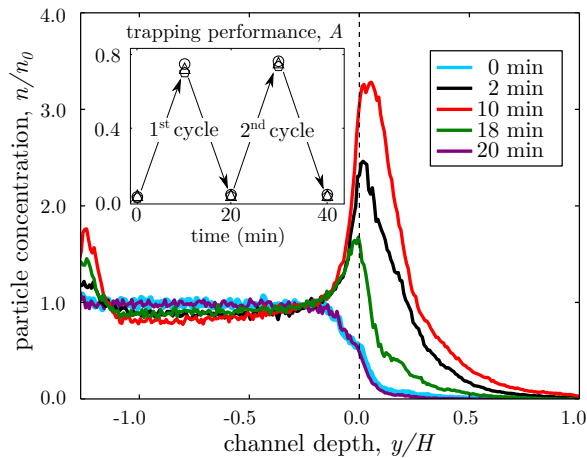


FIG. 5. Reversibility of the particle trapping phenomenon. Time evolution of particle concentration profiles as the colloids are delivered and extracted from the groove by alternating the outer flow between the LiCl solutions at $c_H = 10$ mM and $c_L = 0.1$ mM. Inset: trapping performance of three neighboring grooves during two delivery/extraction cycles.

cordingly over time and return to the initial values at the end of each cycle.

To conclude, this letter demonstrates a new mechanism for reversible trapping of sub-micron particles in dead-end geometries under steady-state gradients. The key ingredients, enabling the fast and steady accumulation of colloids, are the diffusiophoresis migration of particles along the groove depth direction and the flow recirculation region below the groove entrance. Also, the non-vanishing particle velocity in the focusing region prevents sub-micron particles from clustering and permanently clogging the grooves. As a result, the trapping phenomenon is fully reversible and particles can be cyclically trapped and released. We envisage that the proposed mechanism can unlock new opportunities for the exploitation of DP transport in soft matter and living systems for drug delivery, synthetic biology and on-chip diagnostics applications. For example, time-controlled sequential delivery of multiple drugs within dead-end pores could be achieved by switching between flow streams laden with particles having different payloads. On-chip pre-concentration of extracellular microvesicles and cells, followed by sample release and off-chip downstream analysis (e.g. flow cytometry, SEM/TEM) could also be explored.

This research was supported by the EPSRC (EP/S013865/1 and EP/M027341/1) and the Santander Mobility Grant awarded to NS. We thank R. Fulcrand for help with the microdevice manufacturing.

- * g.bolognesi@lboro.ac.uk; www.particlemicrofluidics.com
- [1] A. Kar, T.-Y. Chiang, I. Ortiz Rivera, A. Sen, and D. Velegol, Enhanced transport into and out of dead-end pores, *ACS nano* **9**, 746 (2015).
 - [2] S. Shin, E. Um, B. Sabass, J. T. Ault, M. Rahimi, P. B. Warren, and H. A. Stone, Size-dependent control of colloid transport via solute gradients in dead-end channels, *Proceedings of the National Academy of Sciences* **113**, 257 (2016).
 - [3] S. Shin, P. B. Warren, and H. A. Stone, Cleaning by surfactant gradients: Particulate removal from porous materials and the significance of rinsing in laundry detergency, *Physical Review Applied* **9**, 034012 (2018).
 - [4] B. Abécassis, C. Cottin-Bizonne, C. Ybert, A. Ajdari, and L. Bocquet, Boosting migration of large particles by solute contrasts, *Nature Materials* **7**, 785 (2008).
 - [5] J. Palacci, B. Abécassis, C. Cottin-Bizonne, C. Ybert, and L. Bocquet, Colloidal motility and pattern formation under rectified diffusiophoresis, *Physical Review Letters* **104**, 138302 (2010).
 - [6] N. Shi, R. Nery-Azevedo, A. I. Abdel-Fattah, and T. M. Squires, Diffusiophoretic Focusing of Suspended Colloids, *Physical Review Letters* **117**, 258001 (2016).
 - [7] S. Shin, J. T. Ault, P. B. Warren, and H. A. Stone, Accumulation of colloidal particles in flow junctions induced by fluid flow and diffusiophoresis, *Physical Review X* **7**, 041038 (2017).
 - [8] S. M. Friedrich, J. M. Burke, K. J. Liu, C. F. Ivory, and T.-H. Wang, Molecular rheotaxis directs dna migration and concentration against a pressure-driven flow, *Nature communications* **8**, 1213 (2017).
 - [9] S. Shin, O. Shardt, P. B. Warren, and H. A. Stone, Membraneless water filtration using CO₂, *Nature Communications* **8**, 15181 (2017).
 - [10] D. Ha, S. Seo, K. Lee, and T. Kim, Dynamic transport control of colloidal particles by repeatable active switching of solute gradients, *ACS nano* **13**, 12939 (2019).
 - [11] M. K. Rasmussen, J. N. Pedersen, and R. Marie, Size and surface charge characterization of nanoparticles with a salt gradient, *Nature communications* **11**, 2337 (2020).
 - [12] D. C. Prieve, J. L. Anderson, J. P. Ebel, and M. E. Lowell, Motion of a particle generated by chemical gradients. Part 2. Electrolytes, *Journal of Fluid Mechanics* **148**, 247 (1984).
 - [13] See Supplemental material at url for details on device fabrication, image acquisition and analysis, evaluation of diffusiophoresis coefficient and numerical simulation. Supplemental material includes Refs.[16–19]
 - [14] X. Wu, P. Warszynski, and T. Van de Ven, Electrokinetic lift: Observations and comparisons with theories, *Journal of colloid and interface science* **180**, 61 (1996).
 - [15] R. F. Ismagilov, A. D. Stroock, P. J. Kenis, G. Whitesides, and H. A. Stone, Experimental and theoretical scaling laws for transverse diffusive broadening in two-phase laminar flows in microchannels, *Applied Physics Letters* **76**, 2376 (2000).
 - [16] D. Bartolo, G. Degré, P. Nghe, and V. Studer, Microfluidic stickers, *Lab on a Chip* **8**, 274 (2008).
 - [17] K. Tanaka and M. Nomura, Measurements of tracer diffusion coefficients of lithium ions, chloride ions and water in aqueous lithium chloride solutions, *Journal of the Chem-*

- ical Society, Faraday Transactions 1: Physical Chemistry in Condensed Phases **83**, 1779 (1987).
- [18] R. Mills, The self-diffusion of chloride ion in aqueous alkali chloride solutions at 25, The Journal of Physical Chemistry **61**, 1631 (1957).
- [19] C. Lee, C. Cottin-Bizonne, A.-L. Biance, P. Joseph, L. Bocquet, and C. Ybert, Osmotic flow through fully permeable nanochannels, Physical review letters **112**, 244501 (2014).

Reversible Trapping of Colloids in Microgrooved Channels via Diffusiophoresis under Steady-State Solute Gradients

Naval Singh,¹ Goran T. Vladislavljević,¹ François Nadal,² Cécile Cottin-Bizonne,³ Christophe Pirat,³ and Guido Bolognesi^{1,*}

¹*Department of Chemical Engineering, Loughborough University, Loughborough, LE11 3TU, United Kingdom*

²*Wolfson School of Mechanical, Electrical and Manufacturing Engineering, Loughborough University, Loughborough, LE11 3TU, United Kingdom*

³*Institut Lumière Matière, UMR5306 Université Claude Bernard Lyon 1 - CNRS, Université de Lyon, Villeurbanne Cedex, 69622, France*

(Dated: November 20, 2020)

SUPPLEMENTARY INFORMATION

Device Fabrication and Operation

The Ψ -shaped microchannel is fabricated using standard photo- and soft-lithography processes, such as PDMS replica molding from a negative photoresist SU8-2050 (MicroChem Corp., Newton, USA) master on a silicon surface and microfluidic stickers soft imprint lithography technique [1]. The photo curable thiolene based resin NOA 81 (Norland optical adhesive, USA) patterned mask is prepared from a PDMS (Techsil, UK) mold and partially cured by UV lamp (intensity 3 mW/cm²). The adhesive-imprinted channel is then sealed by UV curing against a microgrooved silicon substrate fabricated by deep reactive ion etching. The dimensions of the channel are width, $w = 400 \mu\text{m}$ and depth, $h = 57 \mu\text{m}$. The dimensions of the microgrooves are thickness, $T = 8 \mu\text{m}$, groove-pitch, $L = 32 \mu\text{m}$ and height, $H = 45 \mu\text{m}$. The total length of the grooved wall is 4 cm, thereby including 1250 grooves in total. Albeit the adhesion is strong, the device is further heated at 80°C for two hours using a hot plate to handle high pressure flows. The inner solution with colloidal particles is supplied by a syringe pump at a flow rate of 12.5 $\mu\text{L}/\text{min}$. The outer flow can be switched between two solutions, as shown in Fig. S1, by means of a flow switching valve. Both solutions are injected by means of a syringe pump at a flow rate of 12.5 $\mu\text{L}/\text{min}$.

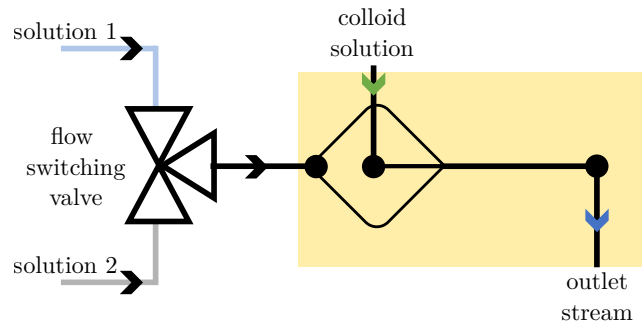


FIG. S1. Device flow configuration. The Ψ -junction device is fed by a colloidal solution for the inner flow and either solution 1 or 2 for the outer flow. A flow switch valve is used to switch the outer flow between solutions 1 and 2.

Image Acquisition and Analysis

Fluorescent colloidal particles concentration recording and imaging are captured using laser scanning confocal microscopy system (Leica TCS SP5, Leica Microsystems) with a 63X Leica water immersion objective (N.A. 1.2, HCX PL APO CS). The excitation wavelength of the dichroic beam splitter is 543 nm and HyD hybrid detector is set between 590 nm and 799 nm. For recording each z-scan, the focus is shifted to the top wall of the microfluidic channel and whole channel is scanned until the bottom of the microgrooves. The colloidal particle distribution is captured as z stack of 512×512 pixels 16-bit TIFF images, acquired at a constant step size (Δz) of 378 nm. A full z-scan acquisition takes approximately 60 seconds. The fluorescence intensity (I) from samples of varying particle

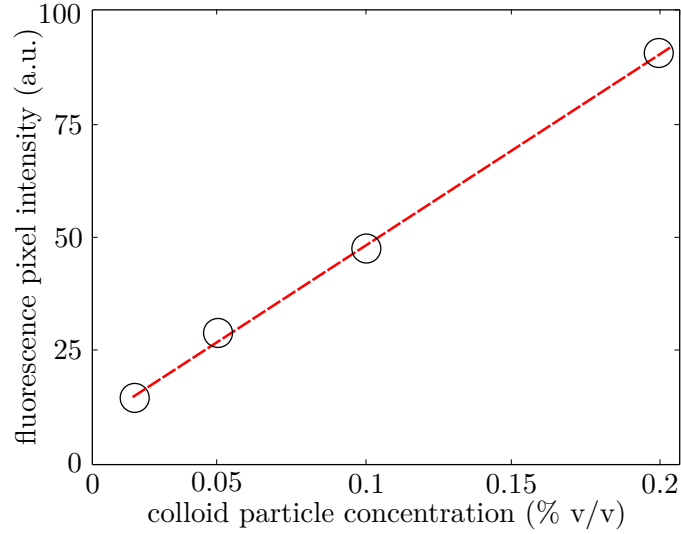


FIG. S2. Confocal microscope calibration curve: particle concentration VS fluorescence intensity.

concentrations n is also recorded and a calibration curve n vs I is determined (Fig. S2). The curve is fitted to a linear function, $I = \alpha n + I_0$, with α and I_0 the fitting parameters.

Evaluation of the Diffusiophoresis Coefficient

Particle diffusiophoresis coefficient is calculated through the formula provided by Prieve and co-workers [2]

$$\Gamma_{\text{DP}} = \frac{\varepsilon}{2\eta} \left(\frac{k_b T}{Z e} \right)^2 [\bar{u}_0 + \bar{u}_1 \lambda + \mathcal{O}(\lambda^2)] \quad (1)$$

with ε the absolute permittivity of the medium, η the medium viscosity, $k_b T$ the thermal energy, Z the ion valence, e the elementary charge and $\lambda = (\kappa a)^{-1}$ is the ratio between the Debye length κ^{-1} and the particle radius a . The Debye length κ^{-1} is given by

$$\kappa^{-1} = \left(\frac{2(Ze)^2 C_\infty}{\varepsilon k_b T} \right)^{1/2} \quad (2)$$

with C_∞ the density number of the solute in the medium. The 0th and 1st order terms in the expansion of Γ_{DP} for small values of λ are given by

$$\bar{u}_0 = 2\beta\bar{\zeta} - 4\ln(1 - \gamma^2) \quad (3)$$

$$\bar{u}_1 = F_0 + \beta F_1 + Pe_D [F_2 + \beta(F_3 + F_5) + \beta^2 F_4] \quad (4)$$

with $\bar{\zeta} = \frac{Ze\zeta}{k_b T}$ the adimensionalised zeta potential, $\gamma = \tanh(\bar{\zeta}/4)$, $\beta = \frac{D_+ - D_-}{D_+ + D_-}$ and D_+ and D_- the diffusivities of cations and anions, respectively. The adimensional number Pe_D is given by

$$Pe_D = \frac{\varepsilon}{2\eta D_s} \left(\frac{k_b T}{Z e} \right)^2 \quad (5)$$

with $D_s = \frac{2D_+ D_-}{D_+ + D_-}$ the salt diffusivity. The functions $F_n(\bar{\zeta})$ are calculated by linearly interpolating the numerical evaluations of F_n functions provided in [2]. Dynamic light scattering and electrophoretic light scattering measurements, performed with an Anton Paar Litesizer 50 instrument, provides an average particle in diameter 215 ± 6 nm and zeta potential of -82 ± 1 mV. By using $D_+ = 1.026 \times 10^{-9}$ m²/s and $D_- = 1.964 \times 10^{-9}$ m²/s for LiCl [3, 4] and $C_\infty \simeq 3$ mM, Eq.(1) gives $\Gamma_{\text{DP}} = 83$ $\mu\text{m}^2/\text{s}$ when second and higher order terms in λ are neglected. Under these conditions, the value of λ is 52.7×10^{-3} .

Numerical Simulations

The 3D computational domain consists in a rectangular channel with a single groove located at a distance z_g from the channel inlet. The following set of dimensionless equations for the hydrodynamic velocity \mathbf{u} , pressure p , salt concentration c and particle concentration n are solved in Comsol Multiphysics

$$\text{Re } \mathbf{u} \cdot \nabla \mathbf{u} = -\nabla p + \nabla^2 \mathbf{u} \quad (6)$$

$$\nabla \cdot \mathbf{u} = 0 \quad (7)$$

$$\text{Pe}_c \mathbf{u} \cdot \nabla c = \nabla^2 c \quad (8)$$

$$\text{Pe}_n \nabla \cdot [(\mathbf{u} + \mathbf{u}_{\text{DP}}) n] = \nabla^2 n \quad \text{with } \mathbf{u}_{\text{DP}} = \xi_{\text{DP}} \frac{\nabla c}{c} \quad (9)$$

with all quantities rescaled according to the following relations

$$u \propto U_0 \quad x, y, z \propto w \quad p \propto \frac{\eta U_0}{w} \quad c \propto c_H \quad n \propto n_0 \quad (10)$$

where U_0 is the average hydrodynamic velocity along the flow direction, w is the actual (dimensional) channel width, η is the viscosity of both outer and inner solutions, c_H is the solute concentration of the outer solution, n_0 is the particle concentration of the inner solution. At the channel inlet, the boundary condition for the velocity field is $\mathbf{u} = \mathbf{u}_{\text{inlet}}$, with $\mathbf{u}_{\text{inlet}}$ the fully developed velocity field at a cross section of the rectangular channel perpendicular to the flow direction and with average velocity equal 1. The boundary conditions at channel inlet for the salt and concentration fields are $c = 1$ and $n = 0$ for the outer flow region and $c = c_L/c_H$ and $n = 1$ for the inner flow region. At the channel outlet, the zero normal gradient boundary condition for the pressure, salt and particle concentrations are imposed. At the remaining walls, the slip boundary condition $\mathbf{u} = -\xi_{\text{DO}} \frac{\nabla c}{c}$ is applied together with the zero flux condition for the salt and particle concentration fields. The channel outlet was located at 5 times the channel depth from the groove to ensure that the boundary conditions at the channel outlet do not affect the fields near the groove. The dimensionless numbers, governing the examined system, are defined as follows

$$\text{Re} = \frac{\rho U_0 w}{\eta} \quad \text{Pe}_c = \frac{w U_0}{D_s} \quad \text{Pe}_n = \frac{w U_0}{D_p} \quad \xi_{\text{DP}} = \frac{\Gamma_{\text{DP}}}{w U_0} \quad \xi_{\text{DO}} = \frac{\Gamma_{\text{DO}}}{w U_0} \quad (11)$$

where ρ is the density of the inner and outer solutions, D_p is the particle diffusivity, calculated as $k_b T / (6\pi\eta a)$, and Γ_{DO} is the diffusioosmosis coefficient of the channel walls. Despite in the experiments the channel walls are made of different materials (namely, silicon for the grooved substrate and optical adhesive glue for the remaining channel walls), a single value of Γ_{DO} is used for all channel walls in the simulations to take advantage of the symmetries of the problem, hence limiting the computational cost. The good agreement between the numerical simulations and experimental results suggests that this assumption is acceptable.

Since the hydrodynamic velocity and salt concentration fields are coupled by the boundary condition for the diffusioosmosis slip velocity, both fields should be solved simultaneously. The resulting finite element computation on a 3D domain would involve a large number of degrees of freedom that would likely require the use of an expensive work station with large memory. Conversely, we can reformulate the problem in order to solve it on a standard PC with 2.7 GHz dual-core processor and 16 GB memory. By using a perturbation approach, the velocity, pressure and salt concentration field are expressed as a power expansion of the parameter ξ_{DO} as follows

$$\mathbf{u} = \mathbf{u}_0 + \xi_{\text{DO}} \mathbf{u}_1 + \mathcal{O}(\xi_{\text{DO}}^2) \quad (12)$$

$$p = p_0 + \xi_{\text{DO}} p_1 + \mathcal{O}(\xi_{\text{DO}}^2) \quad (13)$$

$$c = c_0 + \xi_{\text{DO}} c_1 + \mathcal{O}(\xi_{\text{DO}}^2) \quad (14)$$

The 0th and 1st order terms of the fields are obtained by solving the following equations

$$\text{Re } \mathbf{u}_0 \cdot \nabla \mathbf{u}_0 = -\nabla p_0 + \nabla^2 \mathbf{u}_0 \quad (15)$$

$$\nabla \cdot \mathbf{u}_0 = 0 \quad (16)$$

$$\text{Pe}_c \mathbf{u}_0 \cdot \nabla c_0 = \nabla^2 c_0 \quad (17)$$

$$\text{Re } (\mathbf{u}_1 \cdot \nabla \mathbf{u}_0 + \mathbf{u}_0 \cdot \nabla \mathbf{u}_1) = -\nabla p_1 + \nabla^2 \mathbf{u}_1 \quad (18)$$

$$\nabla \cdot \mathbf{u}_1 = 0 \quad (19)$$

$$\text{Pe}_c (\mathbf{u}_0 \cdot \nabla c_1 + \mathbf{u}_1 \cdot \nabla c_0) = \nabla^2 c_1 \quad (20)$$

The wall boundary conditions for the velocity fields are $u_0 = 0$ and $u_1 = -\nabla c_0 / c_0$. As a results, velocity and concentration fields can be now solved separately in the following order: u_0 , c_0 , u_1 and c_1 . The particle concentration n is determined at last by solving Eq.(9) with the particle diffusiophoresis velocity expressed as

$$\mathbf{u}_{\text{DP}} = \xi_{\text{DP}} \frac{\nabla (c_0 + \xi_{\text{DO}} c_1)}{c_0 + \xi_{\text{DO}} c_1} \quad (21)$$

The numerical results presented in the manuscript are obtained by using the parameters shown in Table S1. The value of Γ_{DO} for the materials of the microchannels used in our experiment is not known, so this parameter is adjusted in order to achieve a good match between experimental and numerical results. The adjusted value of $\Gamma_{\text{DO}} = 375 \mu\text{m}^2/\text{s}$, which corresponds to $\xi_{\text{DO}} = 4.5 \xi_{\text{DP}}$, is of the same order of measured DO coefficients for silicon substrates under similar experimental conditions [5].

Parameter	Value
ρ	10^3 kg/m^3
η	$0.9 \times 10^{-3} \text{ Pa s}$
w	$400 \mu\text{m}$
h	$57 \mu\text{m}$
T	$8 \mu\text{m}$
H	$45 \mu\text{m}$
z_g	4 mm
U_0	18.28 mm/s
c_L	0.1 mM
c_H	10 mM
$2a$	215 nm
Γ_{DP}	$83.2 \mu\text{m}^2/\text{s}$
Γ_{DO}	$375 \mu\text{m}^2/\text{s}$
Re	8.12
Pe _c	5423
Pe _n	3.24×10^6
ξ_{DO}	51.2×10^{-6}
ξ_{DP}	11.4×10^{-6}

TABLE S1. Simulation Parameters

Fig. S3 shows a set of 3D streamlines of the particle velocity field, $\mathbf{u}_p = \mathbf{u} + \mathbf{u}_{\text{DP}}$, starting at the y - z cross section, $x = 0.25$, and at varying depths down the groove. Particles close to the groove entrance can either escape from the groove (blue line) or be caught within the flow recirculation region (green and magenta lines). Particles further down the groove are transported towards the groove entrance due to diffusioosmosis (remaining lines). It is worth noting that these streamlines, calculated by integrating the field \mathbf{u}_p , do not correspond to the actual particle trajectories since the Brownian diffusivity allows particle to move across adjacent flow streamlines.

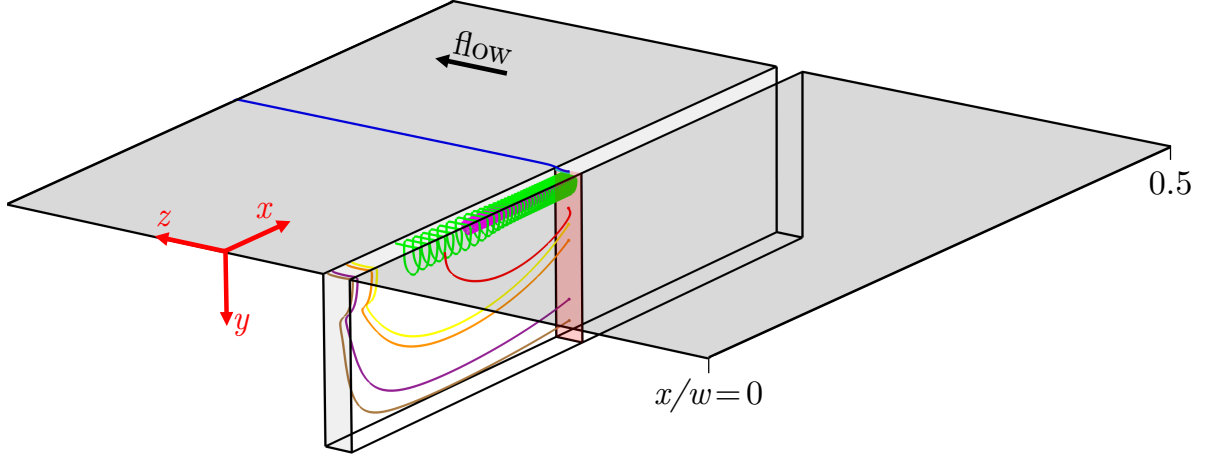


FIG. S3. Groove at 4 mm from the junction and 3D streamlines of the particle velocity, $\mathbf{u}_p = \mathbf{u} + \mathbf{u}_{DP}$, starting from points located at $x/w = 0.25$ (red shaded region) and varying depths down the groove.

Effect of Diffusioosmosis

To clarify the effect of diffusioosmosis (DO) on particle trapping, numerical simulations are performed with different values of the normalized DO coefficient ranging from $\xi_{DO} = 2.5 \xi_{DP}$ to $\xi_{DO} = 6.5 \xi_{DP}$, namely from 28.5×10^{-6} to 74.0×10^{-6} . The corresponding x -/ y -averaged particle concentration profiles along the channel depth (y axis) are shown in Fig.S4. All concentration profiles have a similar shape characterized by a peak located near the entrance of the groove ($y > 0$). Table S2 displays the normalized values of particle concentration peak intensity, n_{max}/n_0 , peak position along channel depth, y_p/H , and peak width, w_p/H – where w_p is the full width at half maximum – for the examined ξ_{DO} values. It can be concluded that, as the value of ξ_{DO} and, hence, the strength of the DO-driven flow increases, the intensity and width of the concentration peak decrease. The narrowing of the peak can be explained by the fact that the peak width is governed by the depth of the recirculation region within the groove, where particle trapping occurs. Since higher DO-driven flows directed from the groove towards the channel, lead to shallower flow recirculation regions, the width of the particle concentration peak also decreases. This interpretation is confirmed by the data in Table S2 showing how the depth of the recirculation region, d_{rec} , decreases for increasing DO coefficient values. Interestingly, the center of the recirculation region is not affected by the DO flow, therefore the location of the concentration peak along the channel depth, y_p , remains unchanged for varying DO coefficients. As shown in Fig.S4, a good match between experimental and theoretical results is achieved for $\xi_{DO} = 4.5 \xi_{DP} = 51.2 \times 10^{-6}$.

TABLE S2. Main properties of the particle concentration peak for varying values of the DO coefficient: n_{max} , peak intensity; y_p , peak position along y (depth) direction; w_p , peak full width at half maximum; d_{rec} , size of the flow recirculation region along y (depth) direction.

$\xi_{DO} \times 10^6$	28.5	51.2	62.6	74.0
n_{max}/n_0	4.75	4.07	3.29	2.56
y_p/H	0.050	0.051	0.050	0.050
w_p/H	0.1081	0.0971	0.0881	0.0781
d_{rec}/H	0.1150	0.0990	0.0975	0.0965

To understand further the role played by diffusioosmosis (DO), numerical simulations are performed also in the absence of DO effects (i.e. $\xi_{DO}=0$). Fig. S5(a) shows the particle concentration at a x -/ y cross section perpendicular to the flow direction whereas Fig. S5(b) show a side view of the particle distribution on a z -/ y plane under these conditions. The corresponding particle concentration profile along the channel depth is shown in Fig. S5(c). Again, a particle concentration peak located just below the groove entrance and at the center of the flow recirculation region ($y_p/H = 0.050$) can be observed, thereby demonstrating that the DO is not required for the discussed particle trapping mechanism to occur. Furthermore, in the absence of a DO flow from the groove towards the channel, particles can

now also accumulate at the bottom of the groove as shown in Fig. S5.

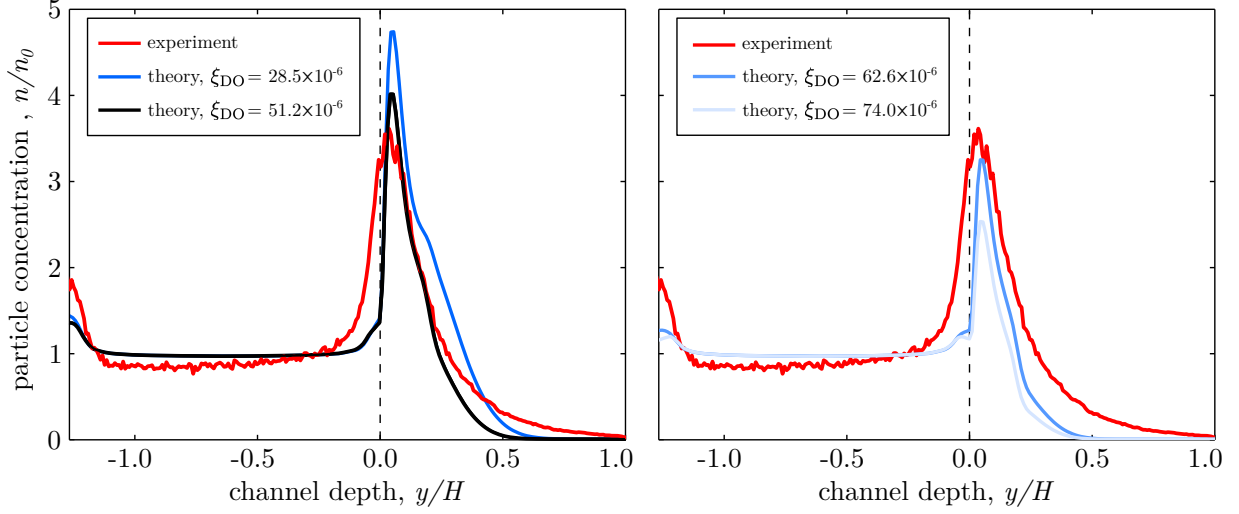


FIG. S4. Numerical predictions for the particle concentration profiles along the channel depth (y axis) for varying DO coefficient values. For sake of comparison, the experimental steady-state profile in Fig.2 of the main manuscript is also shown (red curve).

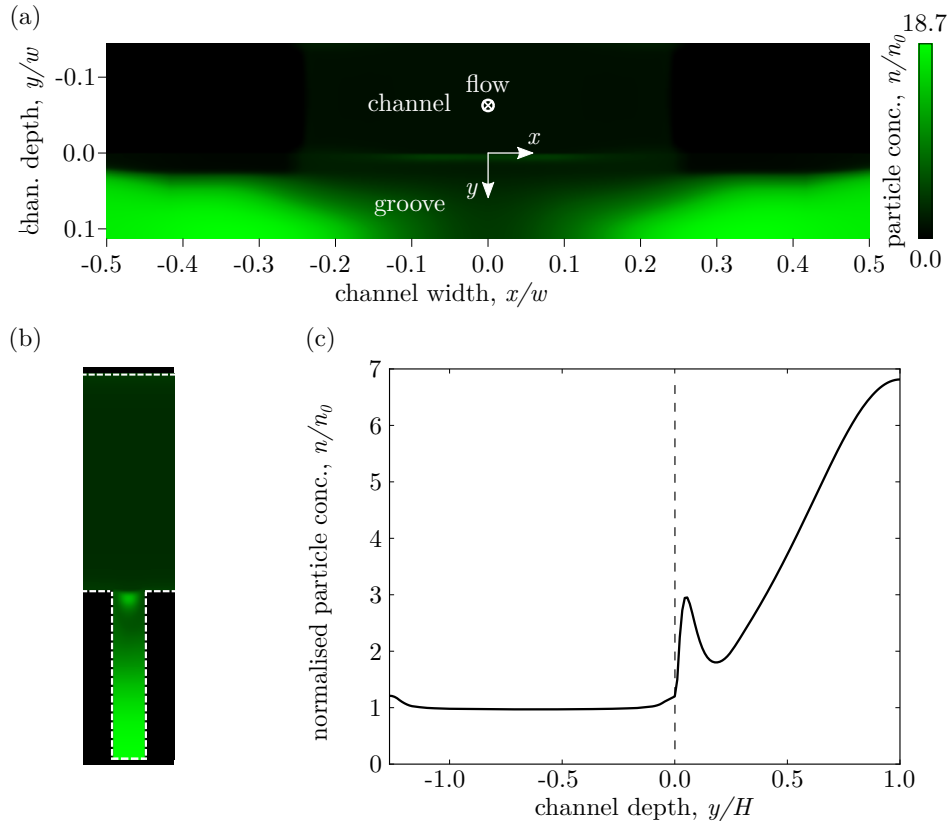


FIG. S5. Simulated particle distribution without DO (i.e., $\xi_{\text{DO}} = 0$). (a) Particle concentration at a x - y cross section, perpendicular to the flow direction z , at 4 mm from the junction. The particle concentration is averaged over the groove thickness T along the z axis. (b) Side view of particle distribution on a z - y plane. The particle concentration is averaged over the channel width direction x . The dashed white lines represent the channel boundaries and groove edges. (c) x -/ y -averaged particle concentration profile along the channel depth (y axis).

Condition for particle focusing

A focusing point corresponds to a local maximum of the particle concentration field, n . At this point of local maximum, the following conditions must be verified

$$\nabla n = 0 \quad (22)$$

$$\text{Tr}(\mathcal{H}) < 0 \quad (23)$$

$$\det(\mathcal{H}) > 0 \quad (24)$$

with \mathcal{H} the Hessian matrix of the field $n(x, y, z)$

$$\mathcal{H} = \begin{pmatrix} \frac{\partial^2 n}{\partial x^2} & \frac{\partial^2 n}{\partial x \partial y} \\ \frac{\partial^2 n}{\partial x \partial y} & \frac{\partial^2 n}{\partial y^2} \end{pmatrix} \quad (25)$$

Eq.(23) and Eq.(24) can hence be rewritten as

$$\nabla^2 n < 0 \quad (26)$$

$$\frac{\partial^2 n}{\partial x^2} \cdot \frac{\partial^2 n}{\partial y^2} - 2 \frac{\partial^2 n}{\partial x \partial y} > 0 \quad (27)$$

From Eq.(9), it follows

$$n \nabla \cdot \mathbf{u} + \mathbf{u} \cdot \nabla n + n \nabla \cdot \mathbf{u}_{\text{DP}} + \mathbf{u}_{\text{DP}} \cdot \nabla n = \frac{1}{\text{Pe}_n} \nabla^2 n \quad (28)$$

Since $\nabla \cdot \mathbf{u} = 0$ and, at the local peak, $\nabla n = 0$, it follows that (for $n \neq 0$)

$$\nabla \cdot \mathbf{u}_{\text{DP}} = \frac{1}{\text{Pe}_n} \frac{\nabla^2 n}{n} < 0 \quad (29)$$

It can be concluded that $\nabla \cdot \mathbf{u}_{\text{DP}} < 0$ is a necessary condition for particle focusing to occur. By denoting the particle velocity as $\mathbf{u}_p = \mathbf{u} + \mathbf{u}_{\text{DP}}$, the same condition can also be expressed as $\nabla \cdot \mathbf{u}_p < 0$.

Interestingly, Eq.(29) can also be re-written in term of a scalar product between the hydrodynamic velocity field \mathbf{u} and the diffusiophoresis velocity field \mathbf{u}_{DP} . Indeed, the divergence of \mathbf{u}_{DP} can be re-written as

$$\nabla \cdot \mathbf{u}_{\text{DP}} = \xi_{\text{DP}} \nabla \cdot \left(\frac{\nabla c}{c} \right) = \frac{\xi_{\text{DP}}}{c} \left(\nabla^2 c - \frac{\nabla c \cdot \nabla c}{c} \right) \quad (30)$$

By replacing the expression for the term $\nabla^2 c$ from Eq.(8), it follows

$$\nabla \cdot \mathbf{u}_{\text{DP}} = \frac{\xi_{\text{DP}}}{c} \left(\text{Pe}_c \mathbf{u} \cdot \nabla c - \frac{\nabla c \cdot \nabla c}{c} \right) = \text{Pe}_c \mathbf{u} \cdot \mathbf{u}_{\text{DP}} - \frac{1}{\xi_{\text{DP}}} \mathbf{u}_{\text{DP}} \cdot \mathbf{u}_{\text{DP}} \quad (31)$$

The necessary condition in Eq.(29) can hence be re-written as

$$\mathbf{u} \cdot \mathbf{u}_{\text{DP}} = \frac{\mathbf{u}_{\text{DP}} \cdot \mathbf{u}_{\text{DP}}}{\xi_{\text{DP}} \text{Pe}_c} = \frac{D_s}{\Gamma_{\text{DP}}} \mathbf{u}_{\text{DP}} \cdot \mathbf{u}_{\text{DP}} \quad (32)$$

By denoting $\hat{\mathbf{u}}_{\text{DP}}$ as the unit vector with the direction of the DP velocity, Eq.(32) can be re-expressed as (for $|\mathbf{u}_{\text{DP}}| \neq 0$)

$$\mathbf{u} \cdot \hat{\mathbf{u}}_{\text{DP}} < \frac{D_s}{\Gamma_{\text{DP}}} |\mathbf{u}_{\text{DP}}| \quad (33)$$

Therefore, at a local peak of the particle concentration field, the component of the hydrodynamic field \mathbf{u} in the direction of the DP velocity \mathbf{u}_{DP} must not exceed $\frac{D_s}{\Gamma_{\text{DP}}}$ times the intensity of the DP velocity.

* g.bolognesi@lboro.ac.uk; www.particlemicrofluidics.com

- [1] D. Bartolo, G. Degré, P. Nghe, and V. Studer, Microfluidic stickers, Lab on a Chip **8**, 274 (2008).
- [2] D. Prieve, J. Anderson, J. Ebel, and M. Lowell, Motion of a particle generated by chemical gradients. part 2. electrolytes, Journal of Fluid Mechanics **148**, 247 (1984).
- [3] K. Tanaka and M. Nomura, Measurements of tracer diffusion coefficients of lithium ions, chloride ions and water in aqueous lithium chloride solutions, Journal of the Chemical Society, Faraday Transactions 1: Physical Chemistry in Condensed Phases **83**, 1779 (1987).
- [4] R. Mills, The self-diffusion of chloride ion in aqueous alkali chloride solutions at 25, The Journal of Physical Chemistry **61**, 1631 (1957).
- [5] C. Lee, C. Cottin-Bizonne, A.-L. Biance, P. Joseph, L. Bocquet, and C. Ybert, Osmotic flow through fully permeable nanochannels, Physical review letters **112**, 244501 (2014).